A new technique for measuring light ion nuclear reactions using TNSA

Mark Yuly, Stephen Padalino, Noah Harley, Andrew Hotchkiss, Chunsun Lei, Andrew Martin.

I. Why use ultrafast high-power lasers to study nuclear science?

With the advent of ultrafast high-power lasers and their deployment at user facilities such as the Laboratory for Laser Energetics (LLE) and the National Ignition Facility (NIF), a new tool has become available for the study of nuclear science. To date, however, nuclear measurements using these types of facilities have mostly focused on experiments where their advantages over traditional particle accelerator techniques are not clear. The overarching goal for the research described in this report is to develop ways to use the distinctive characteristics of ultrafast high-power pulsed laser systems to make nuclear measurements that would be very difficult, if not impossible, using traditional accelerator techniques.

In order to do this, careful consideration of the differences between laser and accelerator experiments is key, and the most productive place to start is most likely where the two techniques differ the most: the length of time over which the nuclear reactions occur.

In an accelerator experiment, a particle beam strikes a target to cause nuclear reactions. These incident particles are travelling in a stream, spread out over a relatively long period of time. For experiments using lasers, however, the situation is markedly different – a single laser pulse of very short duration, picoseconds to nanoseconds, effectively delivers energy to a large number of particles almost instantaneously. In the case of inertial confinement (ICF) experiments, this energy is used to compress the heat a target capsule to the point where thermonuclear reactions can begin to occur. This truly remarkable feat means that, in an instant, for a macroscopic amount of target material, the average thermal energy of the nuclei reaches energies high enough, 10-20 keV, for the nuclei to react with each other. ICF could be used to measure nuclear cross sections for radioactive products by collecting and counting the decays of the product nuclei after the shot. This type of experiment has been the focus of work done over the past seven summers, in which the Short-Lived Isotope Counting System (SLICS) has been developed [1, 2, 3, 4,] and tested in an OMEGA-60 ride-along experiment [5, 6] and by trapping and counting a simulated-ICF neutral radioactive expanding gas [6,7].

Instead of thermal energy, another way to use the laser energy is to accelerate ions using target normal sheath acceleration (TNSA). In this process [8], a laser pre-pulse hits a thin target foil and forms a plasma which can efficiently absorb the energy of the main laser pulse. The energy from the main laser pulse is then transferred to the electrons in the plasma by several mechanisms, causing the electrons to penetrate the foil and pass out of the rear surface. This expanding electron sheath sets up a strong electric field which then accelerates to MeV energies any ions, such as hydrogen or deuterium, present in a surface layer on the rear of the target foil. These ions can then be directed at a nuclear target to cause nuclear reactions.

To understand how this difference in time scale between accelerator and laser experiments affects a measurement of nuclear cross sections, let's look at an activation-type experiment to measure total cross section. In an activation experiment, a nuclear reaction produces a product nucleus that is radioactive. The cross section can be computed from the total number of product nuclei measured by counting the decays of the product nuclei. The rate of decay of the product nuclei (dN/dt) is proportional to the number of product nuclei, N, with the proportionality constant λ, called the decay constant,

$$\frac{dN}{dt} = -\lambda N, \tag{1}$$

which can be integrated to get the classical exponential decay curve

$$N(t) = N_0 e^{-\lambda t} \tag{2}$$

where N_0 is the initial number of product nuclei. The half-life is the time when half the original number are left, $t_{1/2} = \ln 2/\lambda$.

Similarly, bombarding a target with a beam of particles will cause these product nuclei to be formed. The rate at which product nuclei are formed (dN/dt) will be proportional to the number current (number/time) of incident particles, F, and the areal number density (nuclei/area) of the target, T. The constant of proportionality is the total cross section, with units of area. However, as the product nuclei form, they are also decaying away, so

$$\frac{dN}{dt} = \sigma FT - \lambda N. \tag{3}$$

Integrating this yields a growth curve

$$N(t) = \frac{\sigma FT}{\lambda}\left(1 - e^{-\lambda t}\right). \tag{4}$$

where t is the time irradiated.

The typical activation experiment therefore has two phases, the first is when nuclear reactions are occurring and product nuclei are forming ("beam on") and the second when the product nuclei are decaying ("beam off"), and the decays are being counted, as shown in Figure 1. Clearly, when the beam is on the number of product nuclei approaches a maximum value of $N_0 = \sigma FT/\lambda$, above which it can never rise because the nuclei are decaying as fast as they are being created. This means that after a few half-lives, there is very little benefit to more beam time. In order to make a measurement of the cross section, σ, the decay curve, Equation (2), can be fit to the "beam off" decay to obtain the value of N_0, which can then be used to determine σ in Equation (4). The larger N_0 is, the better the statistical uncertainty in the measurement of σ.

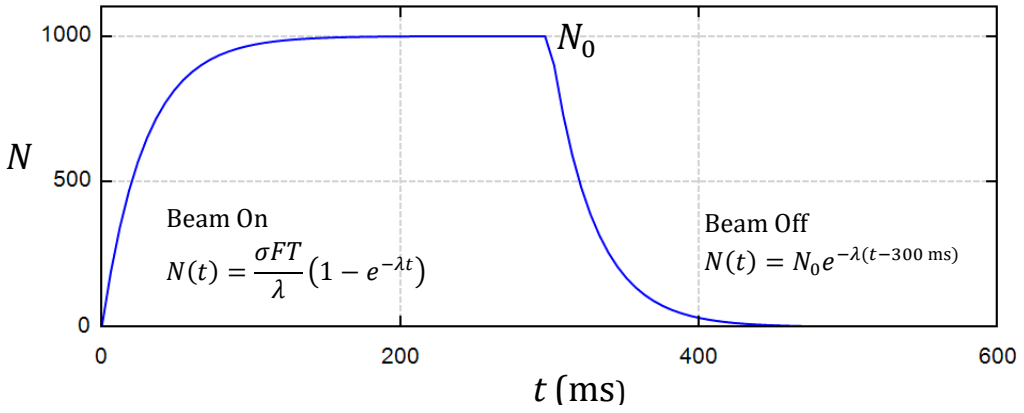

Figure 1. A plot of the number of product nuclei, *N(t)*, as a function of time, *t*. For the first phase, labeled "beam on", the beam is hitting the target causing nuclear reactions and creating reaction products. During the second phase, labeled "beam off", the radioactive product nuclei decay. In this example, both phases last approximately 15 half-lives, so the number reaches very close to the maximum number of product nuclei, $N_0 = \sigma FT/\lambda$.

At this point it is easy to see the difference between the accelerator experiment above, in which the incident particles strike the target over an extend period, and the laser experiment in which the particles interact almost instantly. In the laser experiment, such as those using ICF or TNSA, the second term in Equation (3) disappears – there is essentially no time for the newly created product nuclei to decay. All of the product nuclei are formed at once. On the other hand, in the accelerator experiment the longer the beam is on the less "effective" it is. This means that to get the same statistical uncertainty, the accelerator experiment will require more incident particles.

In accelerator experiments where N_0 is a small number for each pulse, in order to get adequate statistics will require multiple repetitions, which has ramifications for background counts.

In order to demonstrate the ramifications, let's compare a "typical" accelerator experiment with an experiment using TNSA to accelerate deuterons. Table 1 shows typical parameters for comparable accelerator-based and TNSA experiments using the same target, that would produce the same number of product nuclei, about 12,000. In this comparison, a 0.1 μA deuteron beam from an accelerator irradiates the target for three half-lives, so that 3.7×10^{10} deuterons strike the target in each pulse, producing about 19 product nuclei per pulse assuming the given cross section of 0.1 mb. In order to reach 12,000 product nuclei would therefore require 635 beam pulses, or 2.4×10^{13} incident deuterons. For TNSA however, because all of the deuterons hit at once there is no time for the product nuclei to decay, so it requires only about half as many incident deuterons (10^{13}) to make 12,000 reactions.

Table 1. Comparison of accelerator and TNSA activation experiments. The selected parameters give a realistic example of how an accelerator experiment with unacceptable background rates might be doable using TNSA.

Target Parameters		**Using accelerator**	**Quantity**	**Accelerator**	**TNSA**
thickness	2 μm	0.1 μA deuteron beam 60 ms pulses ($3t_{1/2}$) 60 ms counting ($3t_{1/2}$)	Pulse period	120 ms	~60 ms
density	1 g/cm^3		Deuterons/pulse	3.7×10^{10}	10^{13}
cross section	0.1 mb		Repetitions	635	1
weight	10 g/mole		Deuterons on target	2.4×10^{13}	10^{13}
half-life	20 ms	**Using TNSA**	Reactions per pulse	19	12,000
Background		10^{13} deuterons ~ few ns pulse 60 ms counting ($3t_{1/2}$)	Beam related BG	2377 counts	1000 counts
Beam related	10^{-10} /deut		Room background	38,075 counts	60 counts
Room Bkgd.	1000/s		Decay counts	12,044 counts	12,044 counts

The effect of this difference is obvious when background is considered. For the sake of argument, let's look at two types of background. Beam related background refers to background counts proportional to the beam: let's assume every beam deuteron has a one in 10^{-10} chance of producing a background count. Since we count milliseconds after the laser shot, these counts would be mostly due to short half-life activation of materials near the detector. Room background refers to the constant counts coming from cosmic rays and radioactivity in the room. To illustrate, a relatively high estimate of 1000/s was chosen to account for activation of longer-lived isotopes near the detector.

With these assumptions, the accelerator experiment has over twice as many beam related background counts. This is because the accelerator experiment needed over twice as many deuterons to reach the same number of product nuclei, since the product nuclei are decaying while the beam is on. Moreover, because the accelerator experiment requires counting for 635 pulses, the room background is over 38,000 counts for the accelerator experiment, compared to 60 counts for the TNSA experiment. In the accelerator experiment, the decays of the 12,000 product nuclei would be buried in a sea of over 40,000 background counts, whereas for TNSA there would be only a little over 1000 background counts. Careful examination of Equations (2) and (4) reveal that the advantage of TNSA over accelerator measurements increases as the product half-life and cross section decrease.

Another advantage of TNSA is that it could be used to accelerate tritons. Currently there are very few cross section measurements using triton beams because of the radiological hazards involved and the possibility of contaminating the accelerator beamline. However, ICF laboratories are already equipped to handle tritium, and

tritons have successfully been accelerated using TNSA with the OMEGA-EP laser directed into the OMEGA-60 target chamber in "joint shot" configuration [9].

II. How can the SLICS detector be used to measure nuclear cross sections using TNSA?

The SLICS detector system was developed to count the decays of radioactive product nuclei in the expanding gas after an ICF shot, but could also be used to count the beta decays of product nuclei from any TNSA induced reaction leading to a beta emitter with half-live in the range 10 ms to 10 s. In previous experiments [6, 7] the ^{7}Li(d,p)^{8}Li reaction was used to produce ^{8}Li, which, with an 840 ms half-life, would also be a good choice for an intitial TNSA activation experiment. The previous experiments provided experience manufacturing thin lithium films, activating the ^{7}Li with deuterons, and detecting a small amount of ^{8}Li activation on the front face of the SLICS detector. Since all of this would also be helpful in developing a TNSA technique, and since the ^{7}Li(d,p)^{8}Li reaction cross section is relatively large and, as shown in Figure 2, has been previously measured [10-18] down to about 400 keV, it was decided this reaction would be a good starting place. Remarkably, however, it can be seen that there is fairly large disagreement between measurements, which can be used as an argument for the current measurement.

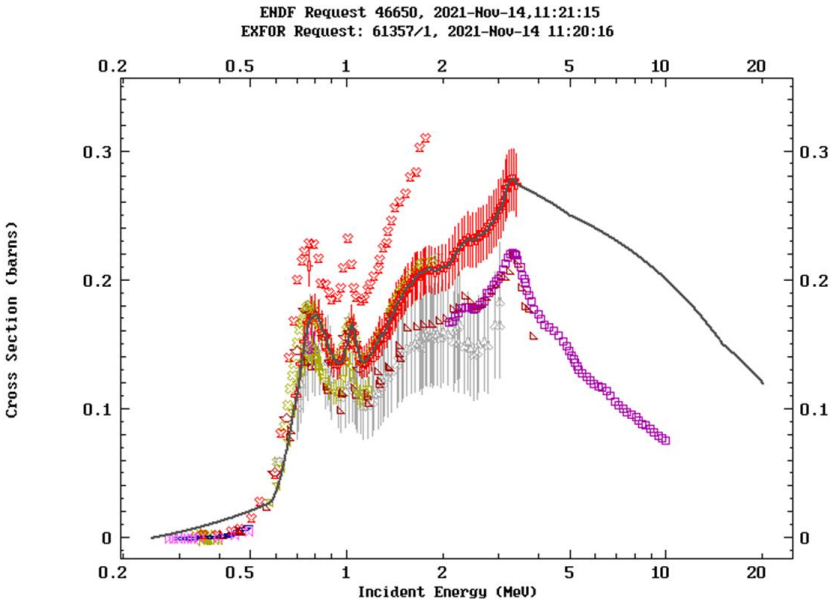

Figure 2. Previous measurements [10-18] of the ^{7}Li(d,p)^{8}Li cross section (symbols) as well as the prediction of the ENDF/B-VIII.0 evaluation (black curve). Plot generated by EXFOR [19].

Figure 2 shows a cartoon diagram a method to measure ^{7}Li(d,p)^{8}Li using TNSA at LLE. A fast, high-power laser pulse from MTW, OMEGA or OMEGA-EP strikes a deuterated polyethylene target to accelerate, using TNSA, a pulse of deuterons, having energies from about 0.2 to 10 MeV. The deuterons then strike a thin natural lithium target where the ^{7}Li(d,p)^{8}Li occurs. The deuterons also strike a small fast plastic scintillator in front of the Li target which measures the time-of-flight (TOF) of the deuterons (and any other ions). The TOF can be used to calculate the energy for a given ion. Since all of the ions hit the TOF detector within about 100 ns, the light is read out through a fiber optic into a distant photomultiplier, and the current is measured using a fast oscilloscope to allow the deuteron energy spectrum to be established. The long fiber optic isolates the electronics from the EMP and prompt radiation.

The beta decays of the ^{8}Li embedded in the Li target are counted by a phoswich detector immediately behind the Li target. The endpoint energy of the beta particle spectrum from ^{8}Li is not well defined because the transition is to a broad excited state of ^{8}Be at 3.03 MeV, but the beta spectrum has its peak at around 6 MeV and extends to energies above 13 MeV [20,21]. For this reason, most of the beta particles easily penetrate the Li target and its substrate, and enter the phoswich detector.

The phoswich detector consists of two layers of plastic scintillator attached to a single light guide and photomultiplier tube in such a way as light from both scintillators reaches the photomultiplier. The front thin dE scintillator is made of plastic that it emits light with a short decay time, while the back thick E scintillator has a much longer decay time. Since the rate that a charged particle loses energy in the scintillator depends on its charge and mass, the light from the two layers can be used to identify the particle and select only beta events.

In order to determine the energy deposited in the dE and E scintillators, the shape of the pulse can be digitized, and integrated with two different windows, a short duration window just around the fast dE pulse, and a much longer window later, once the fast peak has disappeared and all that is left is the long tail of the slow E scintillator. A 2D histogram of dE versus E pulse height measured with these two windows reveals bands for different particle species, so beta events can be selected. For each event the digitizer will also record a time stamp, allowing the beta decay curve to be measured. Fitting the decay curve (Equation (2) with the known efficiency (calculated using a Geant4 [22] simulation) allows the number (N_0) of ^{8}Li to be determined, which then allows the cross section to be determined using Equation (4). In practice, this procedure is complicated by the fact that the incident deuterons are not monoenergetic, so the cross section as a function of energy would need to be deconvoluted from a series of measurements with different deuteron energy spectra. The could be accomplished by varying the thickness of an energy degrader in front of the Li, or by changing the laser parameters.

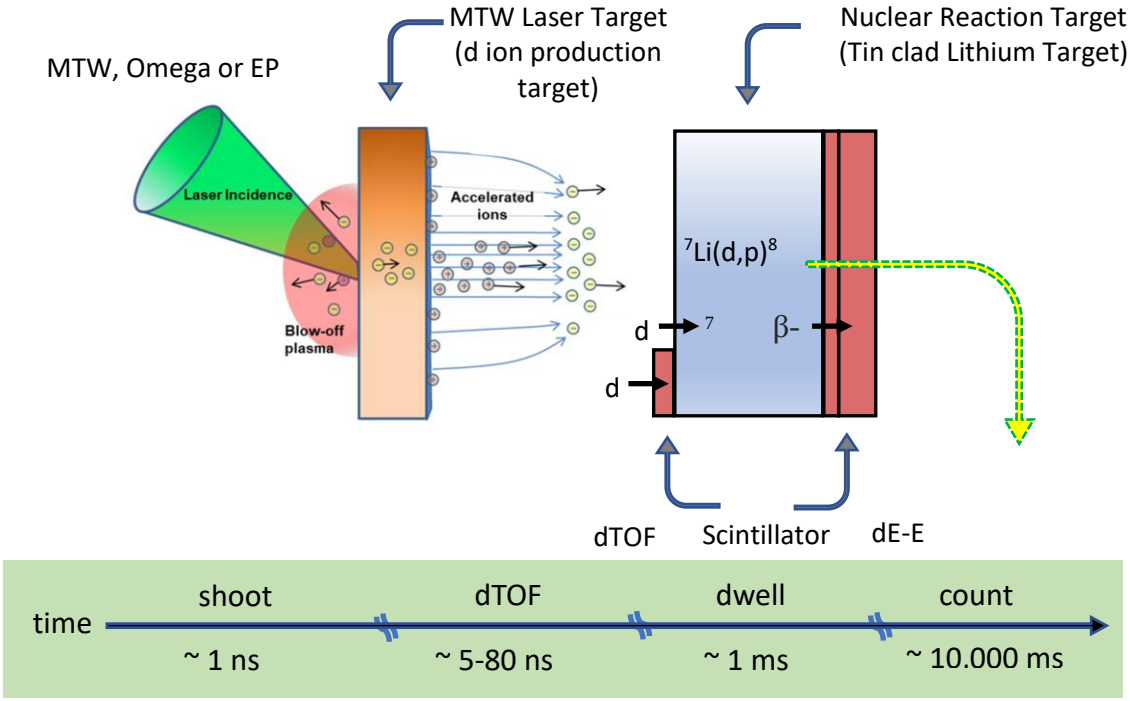

Figure 3. (Top) A cartoon diagram of an experiment to measure the ^{7}Li(d,p)^{8}Li reaction using TNSA deuterons that strike a thin Li target. The beta decay of ^{8}Li is counted by a dE-E phoswich detector. The time-of-flight of the deuterons is recorded using a thin scintillator in front of the Li target. (Bottom) The timeline for the experiment. The initial laser shot accelerates the deuterons in less than 1 ns. The deuterons reach the Li target within about 80 ns, and cause ^{7}Li(d,p)^{8}Li. A few ms later the phoshich detector turns on and begins counting ^{8}Li beta decays for several seconds.

The TNSA deuteron energy spectrum from a deuterated polyethylene target is expected to be very similar to the spectrum from a deuterated titanium target (TiD). Previous experiments using TNSA on MTW measured this spectrum [23, 24] as shown in Figure 4. More protons than deuterons (in addition to various charge states of carbon) are accelerated off the laser target. For a given energy, the protons are moving fastest and reach the TOF detector first, but since there is a spectrum of energies, there will be unavoidable overlap between lower energy protons and higher energy deuterons. However, it appears that below about 0.6 MeV this overlap is minimal, and

hopefully if the shape of the energy distribution is constant, the TOF coupled with periodic Thompson parabola measurements will be adequate to determine the deuteron spectrum for each shot.

The deuteron energy spectrum in Figure 4 was used, along with the cross sections from Figure 2, to make an estimate for the number of ^{7}Li(d,p)^{8}Li reactions that would occur in the Li target in this experiment. To do this, both the cross sections and energy spectrum were fit using cubic splines, and integrated

$$N = \int_{0.25\ \mathrm{MeV}}^{2\ \mathrm{MeV}} Y(E)\,\sigma(E)\,\rho\,t\,\delta\Omega\ \ dE$$

where N is number of reactions, $Y(E)$ is the number of deuterons/MeV/sr striking the lithium metal target, $\sigma(E)$ is the ^{7}Li(d,p)^{8}Li cross section in m^2/sr, ρ is the target number density in Li nuclei/m^3, t is the Li target thickness (2 μm), and $\delta\Omega$ is the solid angle in sr. This yielded an estimate of about 7000 ^{8}Li nuclei produced, which should be detectable.

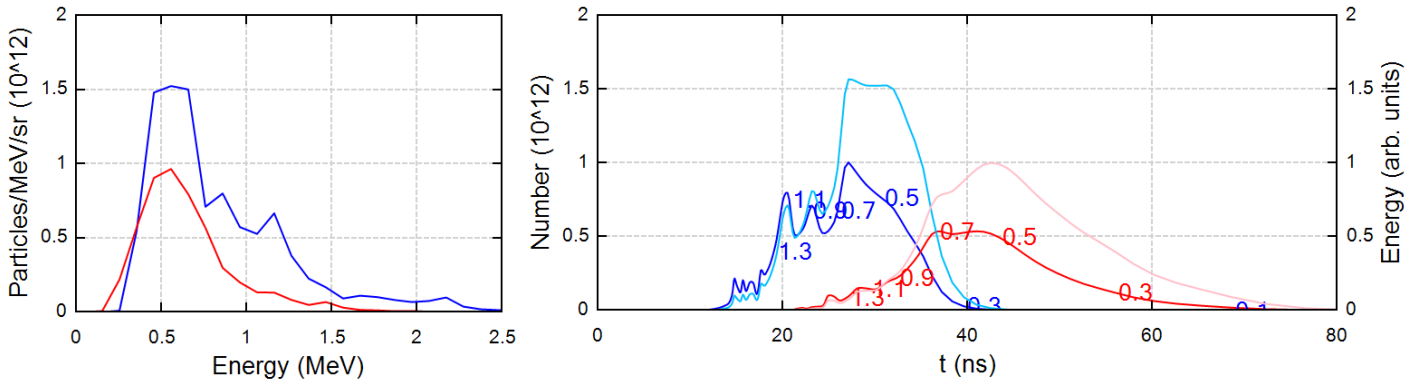

Figure 4. (Left) Energy spectrum for TNSA deuterons (red) and protons (blue) from a TiD target using a 7.3 ps long 22.7 J MTW laser pulse [23]. (Right) The calculated resulting deuteron (red) and proton (blue) TOF spectrum 30 cm from the laser target and the energy deposited in the TOF scintillator by deuterons (light red) and protons (light blue) as a function of the TOF. The numbers represent the approximate location of the corresponding particle energy in MeV.

III. Production and Characterization of Lithium Targets

The lithium targets were made using a specially designed vacuum evaporation system similar to the one described in 2022 [7]. Since it was described earlier, only a brief summary will be given here, along with a more detailed description of the changes since 2022. The deposition system works by running a current through a "boat" to heat a small pellet of lithium in a vacuum. As the lithium evaporates, lithium atoms travel to a substrate where they deposit themselves in a thin film. Once the lithium film of the desired thickness is formed, another boat, containing tin, is heated to form a layer of tin on top of the lithium. In side experiments, attempts were also made to coat the lithium metal with polyethylene and with silver.

The deposition vacuum chamber itself was a 95 mm diameter and 265 mm high stainless-steel cylinder that was evacuated to a base pressure of about 10^{-6} Torr by a 2-inch diffusion pump and a Varian Tri-Scroll forepump. On the side of the cylinder is a 6-inch conflat port which was used to insert the evaporator assembly and feedthroughs for thermocouples. On the bottom and side of the cylinder are flanges that were used for viewports, and on the top a linear positioner allowed the evaporation substrate to be moved vertically by several cm. The pressure in the chamber was monitored using a CCM502 Hornet cold cathode ion gauge and a Lesker 275 convection enhanced Pirani gauge. The vacuum chamber, but not the diffusion pump (which gets hot) was inside a custom-built glove bag that allowed the lithium to be weighed and inserted into the boat, and allowed uncoated lithium films to be removed in an argon atmosphere.

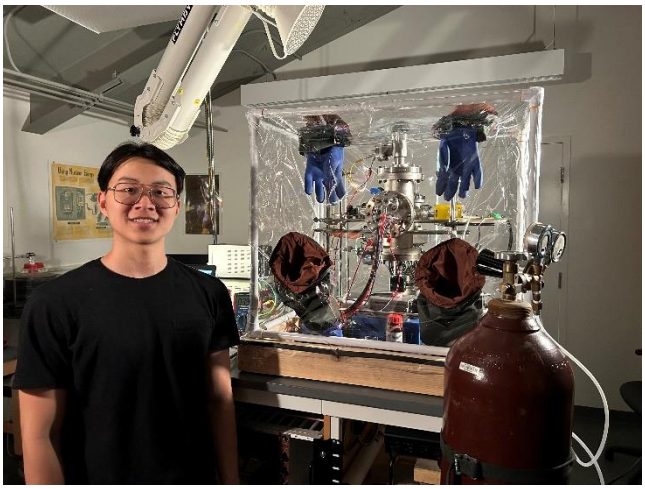

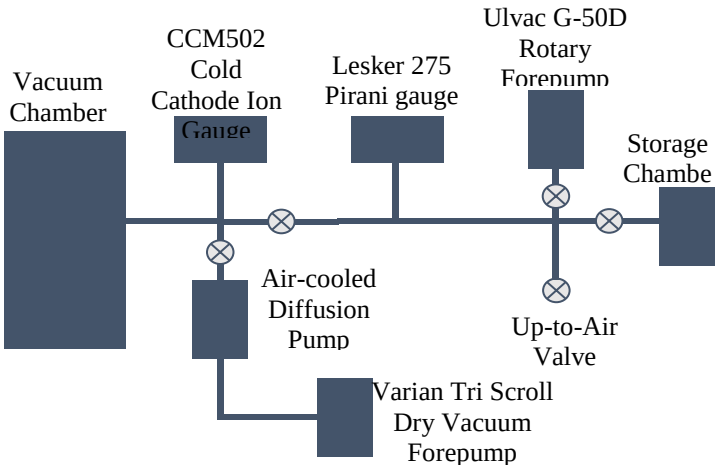

Figure 5. (Left) Houghton University student Chunsun Lei standing in front of his deposition chamber. (Right) Diagram showing the vacuum system for the deposition chamber.

The evaporator is shown in Figure 6. Current from either a 50 A Mastech HY 1550EX or a 60 A CicuitSpecialist CSI-1560 high current power supply flowed into the two-conductor 2.75-inch conflat power feedthrough with ¼ inch rod electrodes. Affixed to these electrodes were two boats, that is, metal strips with a central depression to hold the molten metal. The boat used to evaporate lithium was a hand-made 50 mm long by 15 mm wide by 0.05 mm thick strip of 321 stainless steel, while the tin boat was a 47.6 mm long by 17.1 mm wide by 0.122 mm thick molybdenum strip, Lesker Model EVSME7005MO. The boat to be heated was selected by the direction current flowed using 70HFR120 and 70HF120 70A rectifier diodes. When current flowed one direction, the diodes allowed it to pass through the lithium boat but not the tin boat, when it flowed the opposite direction, the diodes only allowed the current to flow through the tin boat and not the lithium boat. The diodes were in thermal contact with

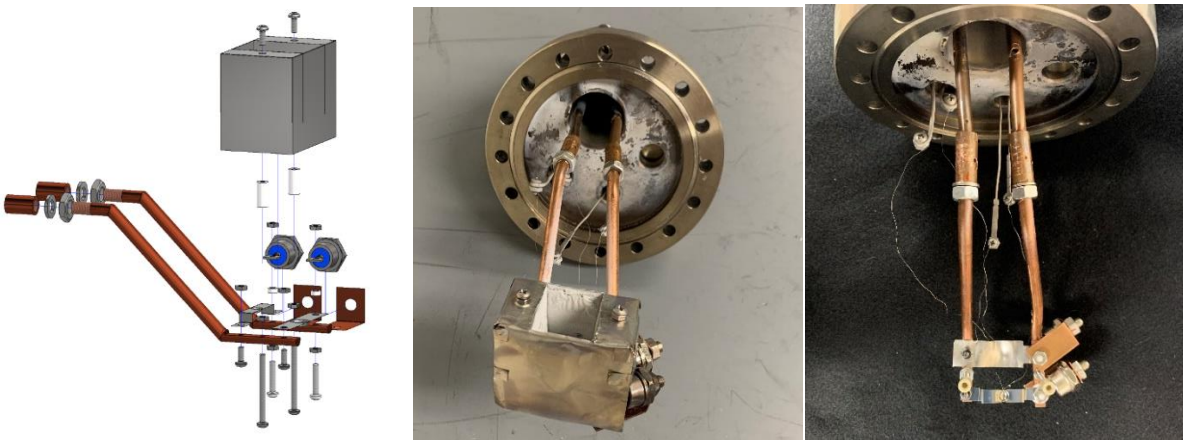

Figure 6. In the exploded drawing of the evaporator (left) a diode circuit controlled which boat is heated. First, one diode allowed current to flow one direction through a stainless-steel boat to heat and evaporate a lithium metal pellet, then another diode allowed current to flow the opposite direction, heating a molybdenum boat to evaporate a tin pellet. A stainless steel "house" surrounded the boats in order to keep the metal, as much as possible, from depositing on the diodes, feedthroughs, and vacuum chamber walls. A photograph (center) of the evaporator with the "house" and with the "house" removed (right) to reveal the boats and diode.

copper strips through which heat flowed into the copper rods and out of the chamber. Two Type-K (Chromel/Alumel) thermocouples were attached to the bottom of the depression on each boat with Rutland Products Furnace Cement allowing the temperatures to be monitored. The boats were surrounded by a stainless steel "house" that is open on top to allow the evaporated atoms to reach the substrate, but kept the metal, as much as possible, from depositing on the diodes, feedthroughs, and vacuum chamber walls.

In order to make a target, the glove bag was first flushed with argon until the oxygen content was less than 4% and the humidity was below about 20% as measured with a Seesii 4 Gas Monitor. Next, an approximately 0.07 g pellet of 99.95% tin was weight, and allowed to slide down a 6 mm diameter aluminum tube into the depression in the molybdenum boat. To do this, the tube was placed so that it entered though the top port of the deposition vacuum chamber, though the open top of the house, and into the depression on the boat. Next, approximately 0.03 g of lithium was weighed out and allowed to slide down the tube into the stainless-steel boat. The substrate was attached to an aluminum cylinder that was screwed to a linear motion feedthrough which was then bolted to the conflat flange on the top port. The system was pumped down to a pressure of approximately 5×10^5 Torr. A current of about 20 A was allowed to flow through the lithium boat, heating it to about 400 °C, for about 20 min. Next, the power supply leads were reversed, and about 50 A was allowed to flow through the tin boat, heating it to about 910 °C for 20 min. After allowing everything to cool, the top port was opened and the coated substrate was removed.

Measuring the thickness of the films was made difficult by the fact that they are conductive coatings on a conductive, non-magnetic substrate. Many of the most common techniques for measuring thickness do not work well for this combination, especially with non-reflective and opaque surfaces. Ultimately, three methods were selected.

Table 2. Methods used to measure the thickness of thin films. Many of these methods do not work well for non-reflective, opaque, conductive films on conductive, non-magnetic substrate. The selected techniques are in various stages of development.

Method	Comment
Eddy Current	Requires a nonconductive film on a conducting substrate.
Dial Gauge	Not very accurate for only a couple micrometer thickness.
Mechanical profilometer	Used this method. May cause deformation, scratching.
Weighing	Lithium is so light it is difficult accurately weigh such thin films.
Deposition rate meter	Hard to incorporate the rate monitor into our deposition system design.
Alpha or beta transmission	Difficult with very thin films on a relatively thick substrate.
Rutherford backscattering	Used this method.
Fluorescence	Need to identify x-ray transitions in the material, hard to calibrate.
Magnetic adhesion	Used this method. Needs a ferromagnetic substrate.
Microscopy	Requires the sample to be sliced to see cross section.
Interferometry	Needs transparent layers and substrate.
Ellipsometry	Needs transparent layers and specular reflection.

A. Magnetic adhesion

The first method, usually called magnetic adhesion [25], is only useable for measuring the thickness of non-magnetic coatings on magnetic substrates. It relies on the decrease in attraction between a magnet and the magnetic substrate due to the increased separation caused by the intervening coating. The strongest force of attraction occurs when the magnet and substrate are in contact. By calibrating the reduced force using coatings with known thickness, an unknown thickness may be measured.

This is the operating principle of the Neoteck NTK 103 thickness gauge, which was used to measure total thickness of the bare lithium and tin-coated lithium films. For this to work, a number of films were produced on SALEX mirror surface 40 mm diameter, 0.5 mm thick magnetic steel discs. This gauge nominally has an accuracy of ($\pm$3% + 2 µm) for thicknesses up to 1500 µm, with a resolution of 0.1 µm. In practice, it was found that for our thin films repeated measurements could vary by as much as 10-20 µm. Moreover, it was very sensitive to the placement of the supporting ring around the tip, and the relatively sharp edges often scratched the surface of the coating.

B. Profilometer

A home-made profilometer was constructed that uses a New Focus 8302 Picomotor Piezo Linear Actuator to move a probe in to touch the conducting sample and substrate, which is mounted on a Yeebyee 150mm Linear Rail Guide. As shown in Figure 7, the picomotor is attached to the base of a 3-axis positioner, which supports the probe. By adjusting the positioner, the probe can be precisely situated relative to the location of interest on the sample. The picomotor works by actuating two piezo-electric crystals that push on an 80 thread-per-inch threaded rod, causing it to move a tiny amount with each pulse of the crystal. This amount varies between about 30 nm/pulse when just starting to about 7 nm/pulse when the threaded rod is moving. The overall rotation of the threaded rod is measured using a Vernier rotary motion sensor, which produces a logic pulse for every 0.25° of radiation. The 12.7 mm diameter shaft of the rotary encoder is turned by a 20.3 mm diameter O-ring covered roller attached to the picomotor threaded rod, giving a resolution of 0.138 nm per tick of the rotary motion encoder. This could be reduced even further by using a different encoder with greater angle resolution.

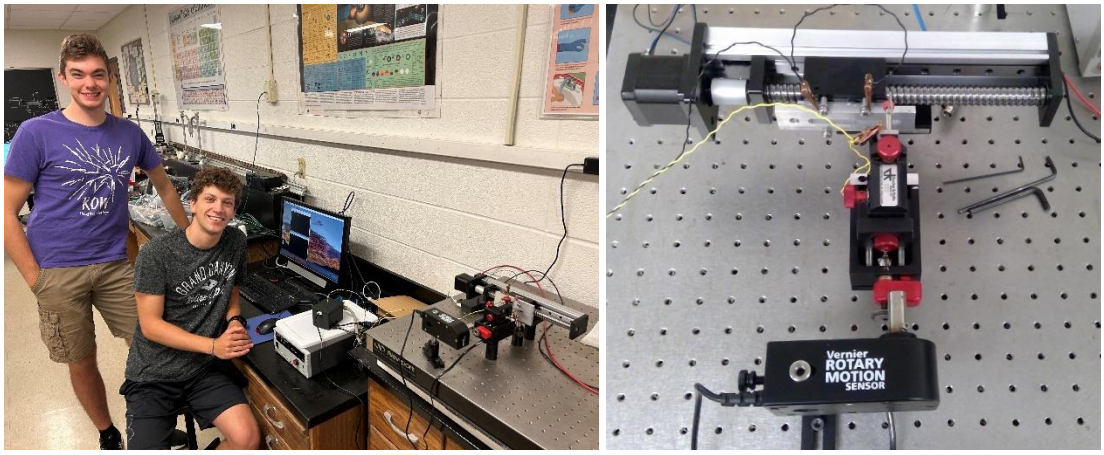

Figure 7. Photographs of Houghton University students Andrew Hotchkiss and Noah Harley with the profilometer (left) and a close-up of the mechanical components (right). The picomotor moves the 3-axis translation stage in and out relative to the coated substrate, which is mounted on the linear stage. The picomotor makes tiny steps inward until the probe tip touches the sample, then steps outward approximately 150 μm at which time the translation stage moves over, and the process begins again. By measuring the angle the picomotor rotated it is possible to determine the distance to the surface with a resolution of about 140 nm.

Figure 8 shows how the profilometer is controlled by a Raspberry Pi 4b using several additional circuit boards attached to its GPIO bus. First, a Lightside Instruments GBIP4Pi board allows the Raspberry Pi to control a GPIB bus to send commands to a New Focus 8732 Multi Axis Driver which in turn sends pulses to move the picomotor. A home-made circuit board converts the 5V pulses from the rotary encoder to 3.3 V needed by the Raspberry Pi, and also allows the electrical contact between the probe and the surface coating to be monitored. A Tic 36v4 stepper motor controller powers the NEMA17 Stepper Motor to move the linear rail guide.

In order to scan the profile of a coated sample, the sample is first clamped into the holder attached to the rail guide, and the probe is placed in the approximate starting position within a few tens of micrometers from the surface. The Raspberry Pi then moves the probe tip in towards the surface in steps of a few nm, each time checking to see if the probe has made electrical contact with the surface. If it has, it records the number of steps and backs out 150 μm. It then moves the linear motion positioner perpendicular to the probe motion, and repeats the process until it has scanned across the entire surface. The relative rotation of the rotary encoder allows the height of the surface above the substrate to be calculated. The rotary encoder is necessary because just counting the number of picomotor pulses is not accurate – the distance traveled per pulse can vary.

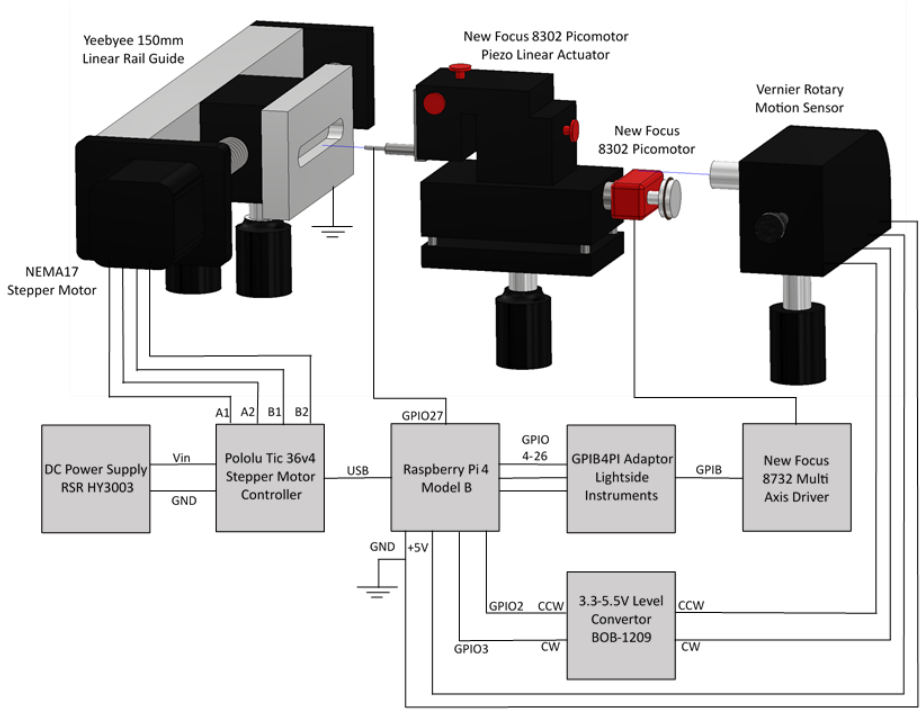

Figure 8. Block diagram of the profilometer. The Raspberry Pi 4 controls the GPIB bus using its GPIO ports and a GPIB4PI board, in order to send commands to the New Focus 8732 Multi Axis Driver to move the New Focus 8302 Picomotor. The Yeebyee 150mm Linear Rail Guide is moved by a stepper motor controlled by the Raspberry Pi over USB with a Tic 36v4 stepper motor controller. When the probe touches the sample, current flows, pulling GPIO 27 low.

Typical results are shown in Figure 9 for both a polished steel gauge block (flat to better than 0.01 μm over its length) and for a substrate covered with a 15.2 μm thick aluminum foil strip and a 25.4 μm thick stainless-steel foil strip. Both are plotted on the same scale for comparison. For the gauge block, the measured height is very consistent, with a standard deviation across the entire surface of about 0.8 μm. This leads to the expectation that it should be possible to measure coatings to sub-micrometer resolution. For the foil covered substrate measurements, a jump of approximately the correct height is present for both foils, although the shape is strange, possibly because the foil is not held tightly against the substrate and might possibly move between measurements. So far measurements of tin-coated substrates have not been successful, presumably because the tin is much softer than the steel probe, which was discovered to have a sharp protrusion that was punching through the tin, as shown in Figure 10. The ensuing scan was essentially flat.

C. Rutherford Backscattering (RBS)

The last method, Rutherford backscattering, has in some ways been the most successful, although it carries with it several limitations. In this method, a beam of 2 MeV protons was allowed to strike the film, and the protons scattered elastically at a backward angle were detected using a silicon detector. From the energy spectrum of the recoiling protons, the thicknesses of film layers can be deduced, assuming the composition of the layers is known. Protons scattered from the front and back of each layer will have different energies because of the energy loss due to travelling through the layer (and the preceding layers) on the way in and out. Protons scattering at a given angle from different layer materials will have different outgoing energies in order to conserve momentum with different

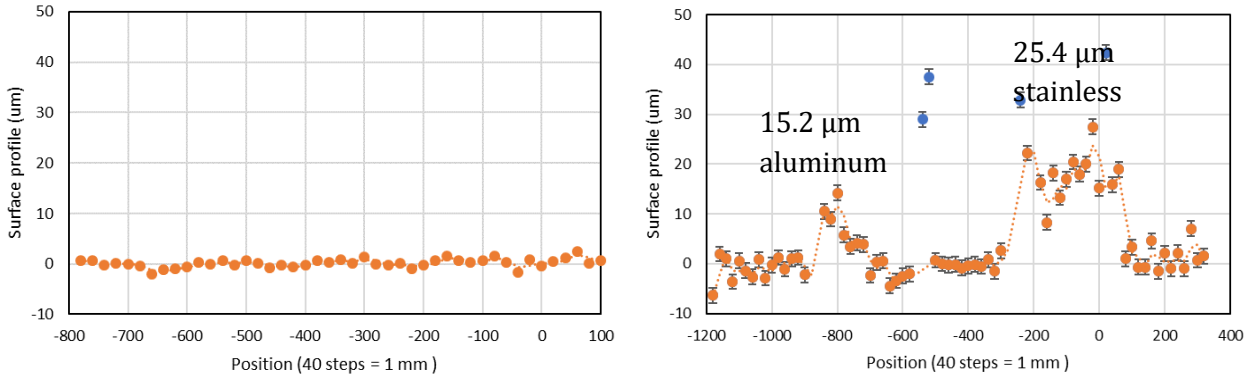

Figure 9. Surface profiles, plotted on the same scale, obtained using the profilometer for a flat steel gauge block (left) and the magnetic steel substrate covered with a 25.4 µm thick stainless-steel foil strip and a 15.2 µm thick aluminum strip (right). The blue symbols were considered outliers.

Figure 10. Micrograph of the tin surface after being in the profilometer. A series of small pinholes is visible where the probe touched the tin surface.

recoiling nuclei masses. This means that by looking at the location and shape of peaks in the energy spectrum, the thickness of the different layers can be reconstructed. Unfortunately, this method requires that the composition of the different layers be known accurately, which means it cannot be easily used with the target consists of a mixture of lithium compounds formed by lithium reacting with air, or unknown alloys formed by two metals interpenetrating. Moreover, because of the kinematics involved, it is difficult to measure low atomic mass layers under heavier layers, which is also the case in this experiment.

The initial test coatings consisted of a single layer of tin of various unknown thicknesses, as shown in Figure 11. Targets 3 and 4 were made first, using the evaporator design from 2022 having a single boat and with the substrate only a couple cm away. Interestingly, the boat for these targets was stainless steel, which is corroded by tin at these temperatures. While the films were forming the boat was destroyed. Targets 1 and 2 were made using the new evaporator with a molybdenum boat, and allowed for a 25.4 mm diameter film to be made. The composition and thickness for Target 3 could not be determined. It was speculated that the tin may have mixed with the stainless steel. The thicknesses for the measure able films ranged between 6.5 nm and 100 nm, which, amazingly is in the desired range based on minimizing the energy loss of the incident deuterons.

The early success at measuring the thickness of tin films alone belied the difficulty of measuring tin coatings on lithium. The initial tin-coated lithium films did not have energy peaks in expected locations, leading to the belief that somehow compounds or alloys had formed. The could be the result of tin alloying with lithium on the surface, or mixing with lithium or other materials (like polyethene) that had previously stuck to the walls of the “house” but were evaporated by the higher temperatures of the tin boat. These questions will be explored in the coming semester.

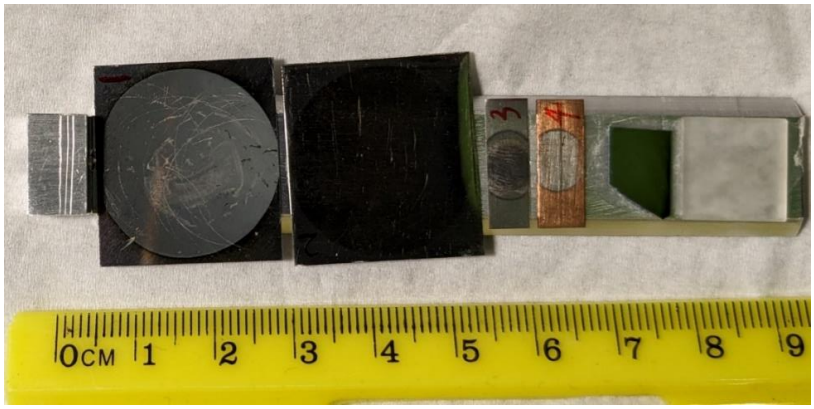

Figure 11. Sn films on the target ladder for measuring with RBS. The measured film thicknesses are as follows: Target 1: Sn on carbon steel, 100 nm; Target 2: Sn on carbon steel, 6.5 nm; Target 3: Sn on stainless steel, no clear signal; Target 4: Sn on Cu 59 nm. The quartz on the target ladder was used to find the beam spot.

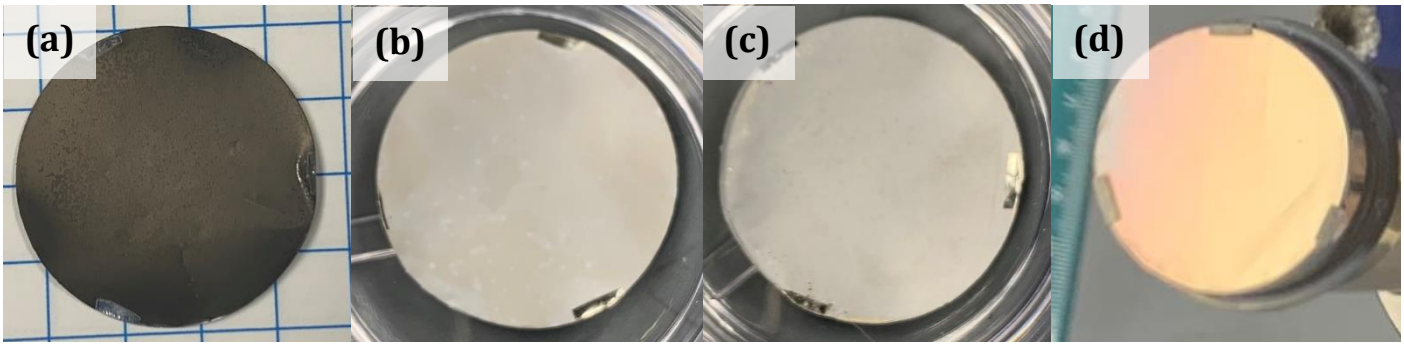

Figure 12. Examples of several films. (a) Tin-coated lithium of unknown thickness, shortly after it was created. A few days later the lithium was oxidized. (b) Pure lithium coating that has oxidized, with some "clumping". (c) Lithium coated with a relatively thick layer of polyethylene, which makes it look "waxy". (d) Silver-coated lithium film immediately after removal. Within about three minutes after this photograph all the lithium reacted with air.

IV. SLICS detector

The detector used in this experiment is very similar to the getter detector that was used in the previous summer's experiments [5, 6], the control electronics including the HV isolation from the 2019 ride along experiment [5] and the CAEN digitizer from 2022 [7]. Since that is the case, a summary will be given here, with the most attention paid to differences from earlier experiments.

The biggest difference from the earlier getter detector is the size – for this experiment, the diameter of the scintillators and light guide was increased to 25.2 mm. As shown in Figure 13, the optical components of the phoswich detector consist of a 1 mm thick, 25.4 mm (1.00 inch) diameter fast EJ-212 scintillator optically coupled using EJ-500 optical epoxy to an 18 mm long, 25.4 mm diameter cylinder of slow EJ-240 scintillator. This assembly was coupled using EJ-500 optical epoxy to a 25.4 mm (nominally 1.025 ± 0.025 inch) diameter, 308 ± 1 mm long Schott F2 glass unclad lightguide. The other end of the lightguide was originally planned to be epoxied with EJ-500 to a 69.9 mm (2.75 inches) diameter, 6.4 mm (0.25 inch) thick Schott F2 glass window.

When gluing the scintillators, it was discovered that it is important to make sure any air in the epoxy is removed prior to the time when the epoxy set. As part of the process for the detector to qualify to be inserted into the MTW target chamber, the materials used in the phoswich detector needed to be tested. A small version of the detector was assembled and put into a test chamber at LLE, in which they were heated to 32 °C (90 °F) and any change in the optical transmission through an optical window was monitored. While no significant changes occurred, when the detector was removed it was "cracked through the bulk of the material". In order to understand what

happened, samples of acrylic, polycarbonate, and different plastic scintillators were epoxied and inserted into a vacuum chamber where they were heated and shocked by quickly opening a valve to evacuate the chamber. Nothing seemed to affect the samples – they all came out with no "cracks.

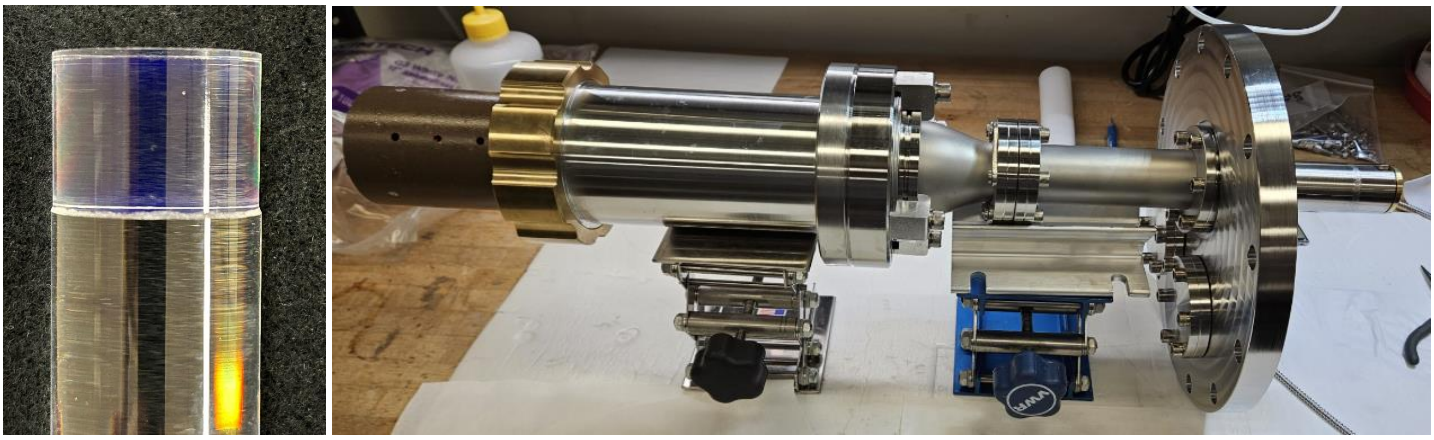

Figure 13. (Left) The thin dE and E detectors were epoxied together and to the glass light guide. (Right) The assembled detector.

Finally, it was remembered that for the detector sent to LLE a step had been skipped. Normally, when gluing the detector, the epoxy is placed into a vacuum prior to it curing in order to remove any dissolved or trapped air. This is done to remove any bubbles that might absorb the light. Since this detector was not going to be used to collect light this step was skipped. In order to test if this was the problem, another test scintillator detector was built but the vacuum-bubble step was skipped. When this detector was put into the vacuum chamber, lots of "cracks" appeared, as seen in Figure 14.

This entire optical assembly was inserted into a stainless-steel tube, as shown in Figure 13, Figure 15, and Figure 16. A flange on one end of the tube made a vacuum seal against the glass window using a rubber O-ring. On the other end of the tube, the lithium target on a 25.4 μm thick 25.4 mm diameter stainless steel foil was placed against the dE scintillator and held in place with a retaining ring. On the other side of the glass window, an RCA/Burle 7585 photomultiplier tube (PMT) was held firmly in place by a holder that uses a compression ring to support the ORTEC 265A PMT base. The optical coupling between the lightguide and phototube was made using EJ-550 optical silicone grease.

Figure 14. (Left) Photograph of the small phoswich detector that was sent to LLE to test for outgassing. After the detector was removed from the vacuum, small cracks were discovered. (Center and Right) Photographs of phoswich detector after removing it from the test vacuum chamber at Houghton University for a detector that was glued with epoxy that had air in it.

On the other side of the nuclear target from the phoswich scintillators was planned to be the TOF detector, which consisted of a 1/16th pie wedge of a 25.4 mm (1 inch) diameter circle of 1 mm thick EJ-200 plastic scintillator. This

scintillator was planned to be supported from the edge by a fiber optic connector that went through a notch in the end of the stainless-steel tube. A fiber optic was attached which went out through a vacuum feedthrough on a separate port. The fiber optic was inside a steel protective sheath.

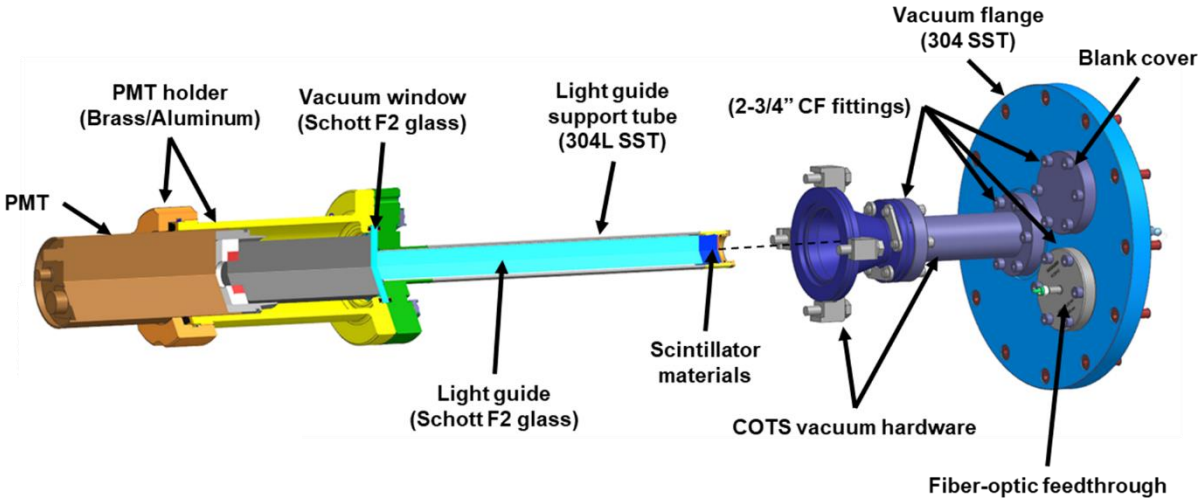

Figure 15. The SLICS detector assembly. On one end of the glass lightguide the phoswich scintillators were epoxied, and the other end was designed to be epoxied to a glass window. This entire optical assembly was inserted into a stainless-steel tube that provided support allowing the detector to extend into the target chamber if desired. A flange at the end of the tube created a vacuum seal with the glass window, the other side of which was in optical contact with the PMT. The distance of the phoswich detector from the laser target could be changed by inserting different length full nipples.

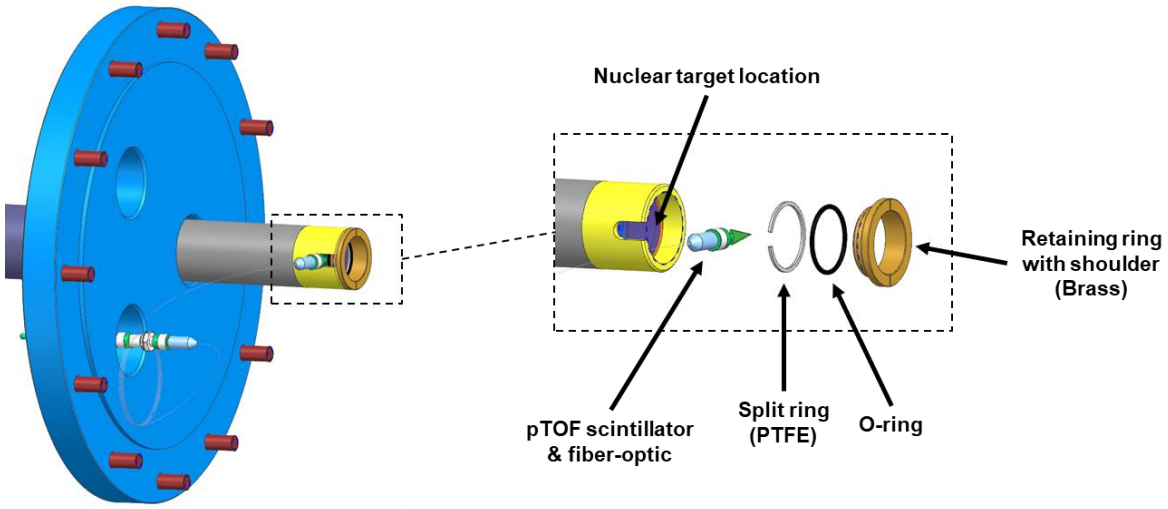

Figure 16. Detail diagram showing the end of the SLICS detector. The phoswich detector was attached to the glass light guide at the end of the detector closest to the laser target. The thin lithium target was held against the phoswich detector by a retaining ring set. In front of the lithium target. As originally planned, the TOF scintillator was attached to a fiber optic that runs to a feedthrough on another vacuum port.

The electronics block diagram for the phoswich detector is shown in Figure 17. A 400 ns long TTL pulse from the MTW laser control system indicated a laser shot. The pulse was converted to a 3.3 V logic pulse by the ORTEC gate generator in order to be compatible with the GPIO inputs of the Raspberry Pi 4 single board computer that controlled the timing of the experiment. A few milliseconds after the leading edge of the MTW shot pulse, the

Raspberry Pi powered up the PMT and connected the signal to the digitizers, which were isolated by HV relays to protect them from the EMP and prompt radiation. To do this, the Raspberry Pi turned on MOSFETS, which power the relay coil.

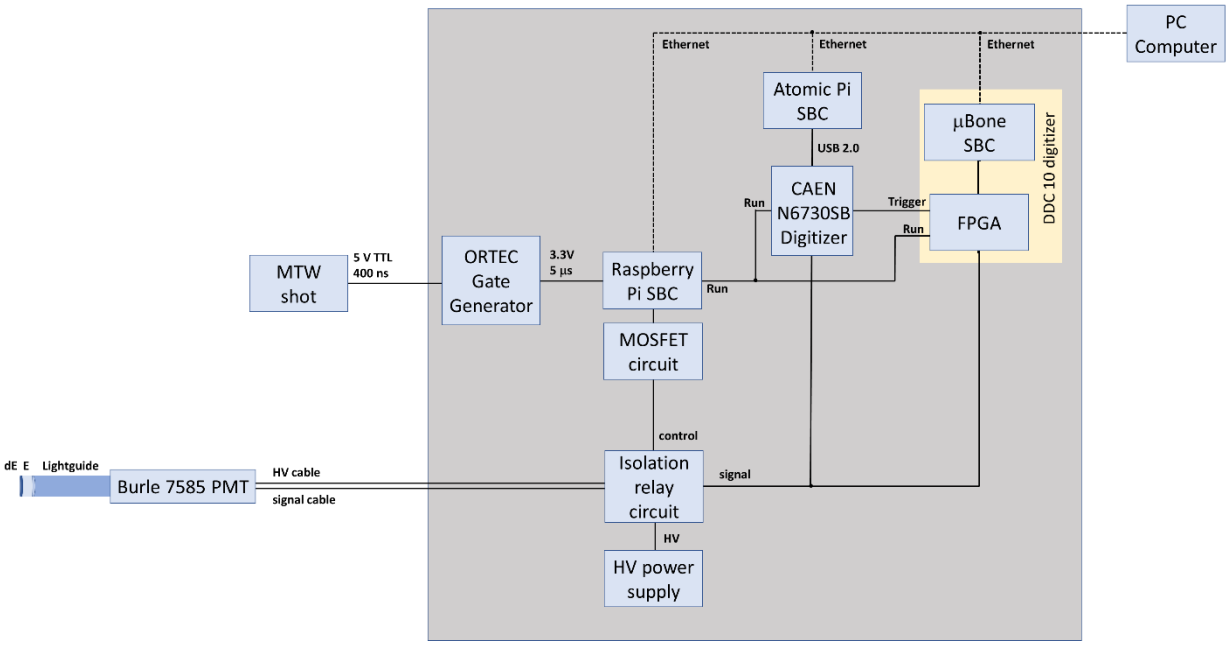

Figure 17. Block diagram of electronics. A signal from the MTW laser indicated the laser shot had occurred. The signal was converted from TTL to 3.3 V logic using the ORTEC gate generator. The leading edge of this signal caused the Raspberry Pi 4, which controlled the timing of the experiment, to begin powering up the PMT after a few milliseconds, after the prompt radiation and EMP had passed. This was done using a MOSFET circuit to energize HV isolation relays on both the signal, HV and ground for the PMT. The Raspberry Pi then started both the CAEN and DDC 10 digitizers. The trigger generated by the CAEN digitizer was used to trigger the DDC 10, ensuring the same events were digitized.

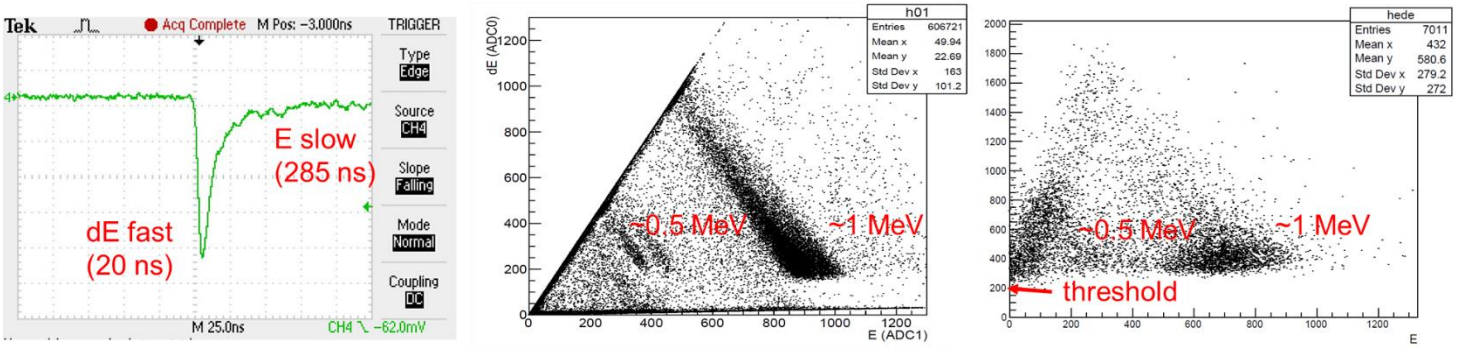

Figure 18. Performance of the detector with a ^{207}Bi monoenergetic electron source directly in front of the detector. (Left) A typical beta pulse from the PMT, showing the fast and slow components due to the thin EJ-212 dE scintillator and thick EJ-240 E scintillator, with decay times of 2.4 ns and 285 ns, respectively. (Center) A 2D histogram of the energy deposited in the dE and E scintillators predicted by a Geant4 simulation with realistic cross talk. (Right) The measured 2D histogram, with the trigger threshold set to approximately channel 250 on the dE signal. The ^{207}Bi source emits monoenergetic electrons with energies of about 0.5 MeV and 1 MeV, superimposed on a beta spectrum.

V. Experiment at MTW

The experiment that was carried out using the MTW laser during the summer of 2023 was intended to be a shakedown of the SLICS detector system and a test of the feasibility of the concept of using TNSA to measure light-

ion cross sections. The week prior to the shot week, several days were allotted for setting up and testing the detector systems. The Monday of the shot week was planned for tuning up the MTW laser, and the remaining four days were allotted for the experiment.

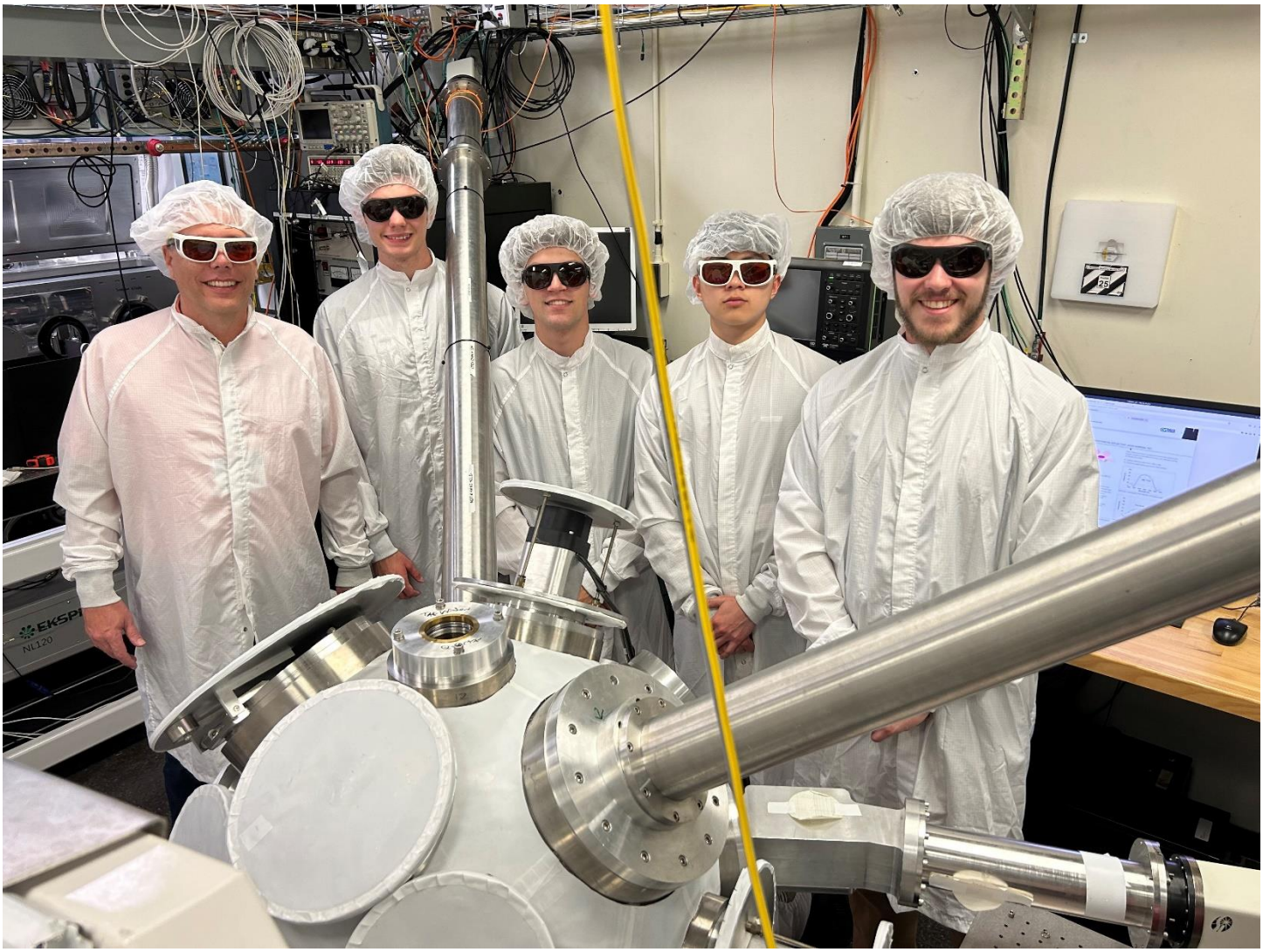

Figure 19. (Left to right) Houghton professor Mark Yuly with students Andrew Hotchkiss, Noah Harley, Chunsun Lei, and Andrew Martin preparing for their first experiment using the MTW laser.

Prior to arriving at LLE on July 19, the detector had been assembled as part of the "Fit and Function" test, and attached to the MTW target chamber which was pumped down to a pressure of about 10^{-5} Torr, which took about 12 minutes. Unfortunately, the main detector tube needed to be sent for passivation, and the final optical joint between the light guide and the glass window was unable to be made beforehand at Houghton University. As part of this test, it was also discovered that the TOF detector epoxy joint was likely not strong enough to support the fiber optic cable when it was handled.

One anticipated problem was the large light leak introduced by the slot cut into the end of the tube to allow the TOF scintillator to be inserted. The plan was that the scintillators would be covered by a thin opaque aluminized mylar sheath before being inserted into the tube. During the "Fit and Function" test, however, it was discovered that the clearance between the threaded end of the tube and the scintillators was less than expected. Nevertheless, four sheets of very thin, almost-opaque mylar were used to cover the scintillators and block almost all of the light. Unfortunately, four sheets was not quite enough to stop all the light, so, in the end, the decision was made to mylar tape over the notch and reverse the order of the Teflon split ring and Viton O-ring, which completely eliminated the

light leakage. Since the TOF detector could no longer be inserted into the end of the detector tube, the TOF scintillator was attached to the tube with a special clamp, shown in Figure 22.

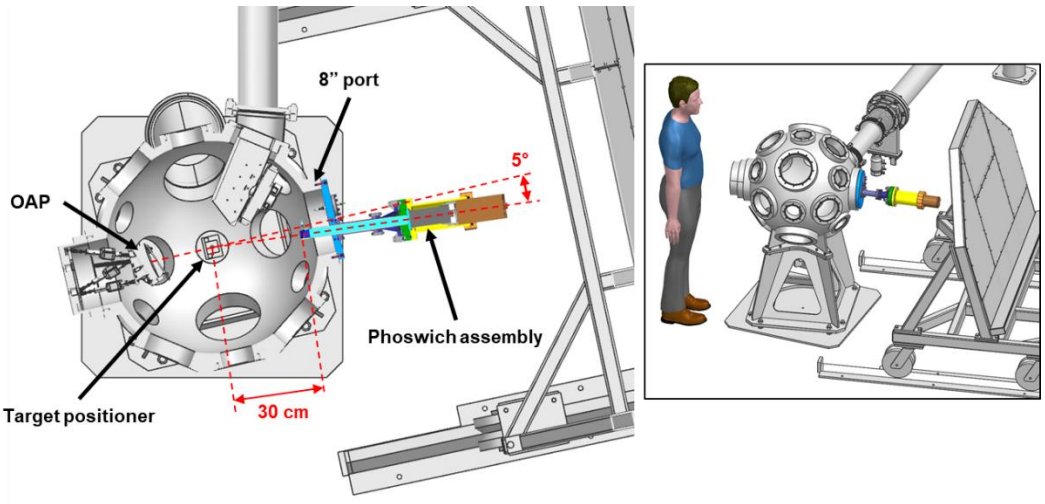

Figure 20. The SLICS detector was attached to the MTW chamber port directly opposite the off-axis parabola, but was offset so that it pointed toward the laser target from 5° off the laser beam path. The shield wall was directly behind the SLICS detector.

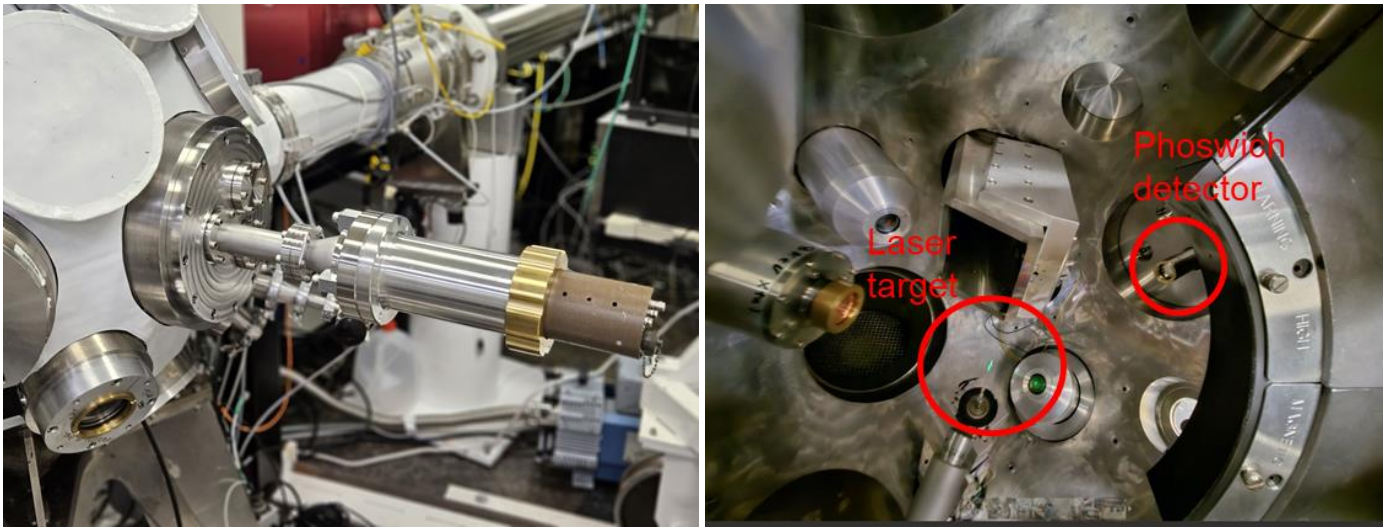

Figure 21. (Left) Photograph of the SLICS detector attached to the MTW target chamber. (Right) Photograph of the inside of the MTW chamber, showing the position of the nuclear target and phoswich detector relative to the laser target.

Since the scintillators fit so snugly into the end of the tube, there was concern that it may not be possible to make the end of the lightguide and the glass window have perfectly parallel surfaces for the epoxy joint. Since this was to be a permanent joint and no spare lightguide was available, any mistakes would leave the detector unusable. For this reason, two tests were made. First, the detector was assembled with the bare glass surfaces in contact to see if enough light would be transmitted that the gluing step could be eliminated. Second, the EJ-550 optical silicone grease was tested in the LLE test chamber and it was found allowable to put into the MTW chamber. With just the bare glass interface it was possible to identify electrons from the ^{207}Bi source. When EJ-550 optical grease was added to the joint between the window and the phototube there was no appreciable change, so the decision was made to just keep bare glass-to-glass contact for the joint between the light guide and the window.

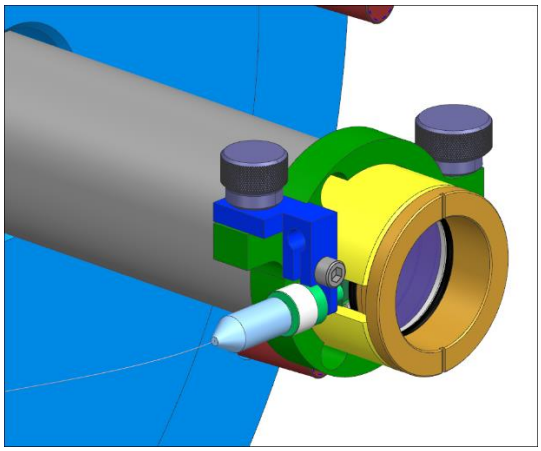

Figure 22. A Delrin holder was made to clamp onto the tube and hold the TOF detector. It was discovered that by rotating the clamp the scintillator could be oriented to be in front of the nuclear target.

As often seems to be the case in physics experiments, on the very first laser shot of the experiment, the HV isolation relay circuit, which had worked perfectly in all of the preliminary tests in the nuclear lab and in MTW, stopped functioning. Given the time constraints, and since in previous MTW experiments oscilloscopes and phototubes at about the same distance have remained undamaged, it was decided to remove the HV relay system entirely, and directly connect the photomultiplier high voltage and signal.

A. Initial tests of SLICS and TOF system

The phoswich detector response of the first working laser shot (shot #15974, Run 4), using the CAEN digitizer, is shown in Figure 23. This was a 10 J, 10 ps laser shot on a deuterated polyethylene target, with a 6 μm thick target of natural lithium oxide. A very clear band of good beta events was seen, and these events were selected and the number histogramed as a function of time. A large peak in the number was seen on the time spectrum for times less than about 200 ms, after which the number of beta events decayed with a half-life of about 840 ms, as expected for ^{8}Li. Interestingly, the selecting the events within the "noise" blob seems to correspond to the peak at short times. Selecting just those events on the 2D histogram gives the time spectrum shown in Figure 24.

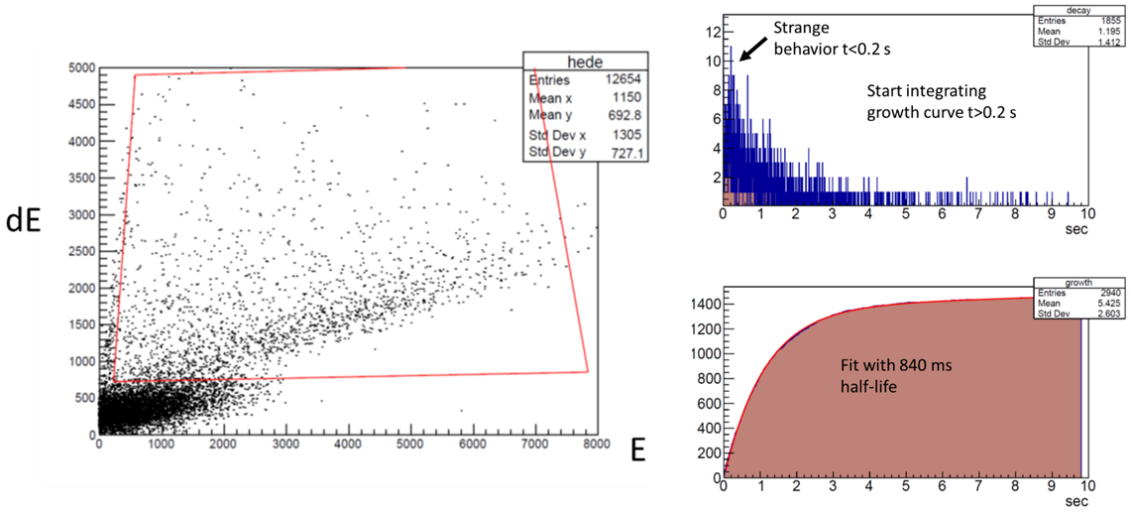

Figure 23. (Left) 2D histogram showing the dE detector pulse height versus the E detector pulse height. The events within the red box were counted as good beta events. The source of the dark "noise" blob near the origin is unknown. (Right top) Histogram of the selected beta events as a function of time, in 3.3 ms time bins. There was a large peak for times less than about 200 ms, after which there is a visible decay curve. (Right bottom) The growth curve was created by integrating from 200 ms onward. The red curve shows a fit of the exponential growth curve plus constant background, with fixed half-life of 840 ms.

Laser shots were performed with several permutations of laser and nuclear targets, in order to convincingly establish the source of the 840 ms decay curve that was obtained in the first laser shot. As shown in Figure 25, the laser shot with the CD laser target and the 9 μm natural lithium oxide nuclear target found 5742 events that fell within the "good beta event" window (red box) on the 2D particle identificaiton dE-E histogram. Fitting the growth curve yields a total number of ^{8}Li that would be detected in the time after 200 ms to be 5153. The reason for the discrepancy is that times before 200 ms are ignored in the growth curve fit, and times after 10 sec are ignored in the particle identificaiton cut.

Figure 25 also shows the same histograms, but for the laser shot with the CH_2 laser target. From this target protons but no deuterons were expected, so there would not be any ^{7}Li(d,p)^{8}Li reactions and hence no ^{8}Li beta decay electrons. Indeed, this was exactly what was observed – the number of good beta events in the red selection window on the 2D particle identification histogram fell to 13, and the growth curve is linear as well as can be determined fom such a small number of events.

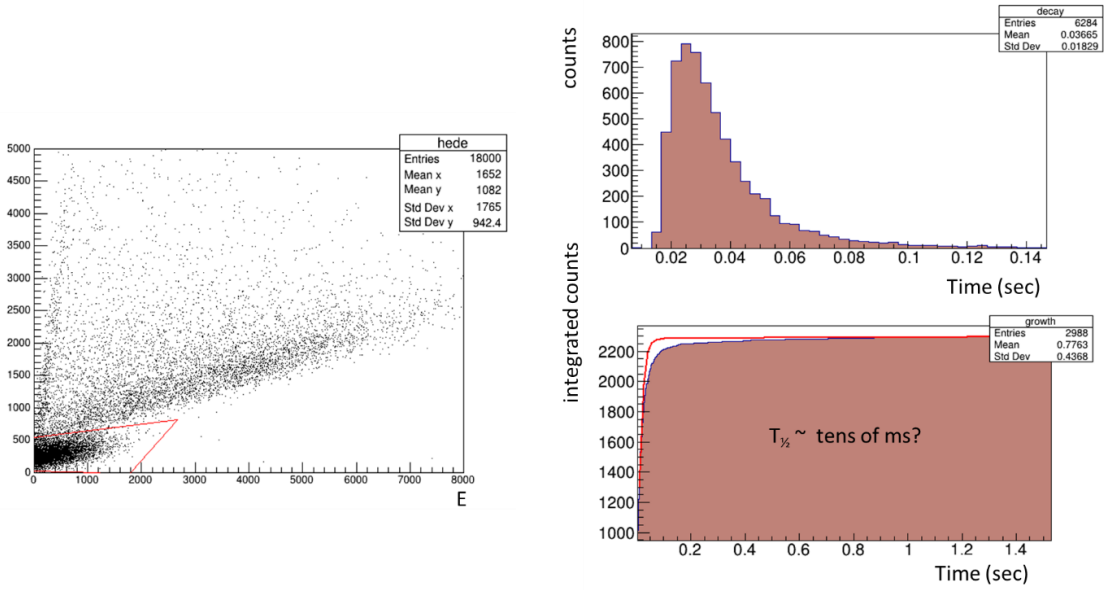

Figure 24. Selecting events in the "noise" (left) results in a time spectrum peaked at about 30 ms (right top) that seems to decay exponentially with time. Integrating the decay curve yields a growth curve (right bottom) that seems to have a half-life of a few seconds, but that was unable to be fit with a single exponential growth function.

Finally, a laser shot with the CD laser target and a blank (no lithium) nuclear target is also shown in Figure 25. In this case, it was also expected that no ^{7}Li(d,p)^{8}Li reactions would occur because there was no lithium. This was also observed, with no lithium target the number of good beta events fell to 127. Interestingly, these events seemed to decay with a half-life of a few seconds; however, because of the low statistics it was not possible to fit the growth curve. It may also be the case that the decay is not exponetial, or may have more than a single component.

With these results it is safe to say that we have used TNSA on MTW to accelerate deuterons that then caused the ^{7}Li(d,p)^{8}Li reaction to occur in a thin lithium oxide target. We detected the ^{8}Li beta decays and were able to fit the growth curve and determine the number of detected ^{8}Li decays. When combined with the efficiency determined from the Geant simulation this will give the number of ^{8}Li product nuclei that were produced.

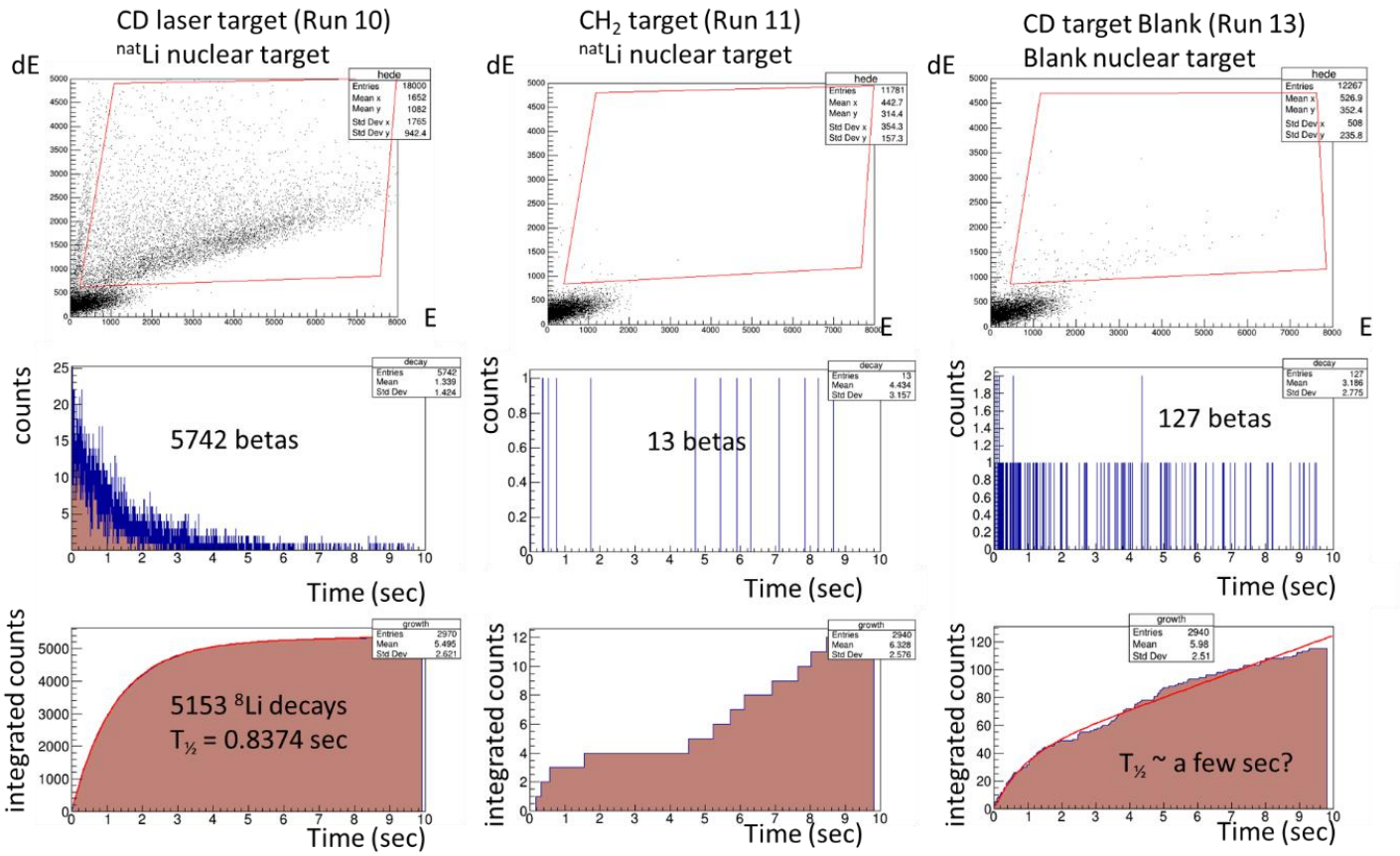

Figure 25. Summary of the results, for the CD laser target with a 9 μm thick natural lithium oxide target (left column), CH_2 laser target with a 9 μm thick natural lithium oxide target (center column), and CD laser target with a blank natural target (right column). The top row shows the 2D particle identification histogram with selected good beta events , the second row is the time spectrum for those good beta events, and the bottom row shows the intergrated time spectrum (growth curve) and fit parameters.

VI. Future Plans

The experiments this summer will help to better understand the detector and the problems that arise in this type of activation experiment using TNSA. Based on the results, a possible plan for future experiments might look like the following:

Early 2024 OMEGA ride along background measurement
Summer 2024 MTW TNSA production measurement of $^{7}Li(d,p)^{8}Li$
Summer 2025 OMEGA-60 ride along for high-yield tritium filled target $^{3}H(t,\gamma)^{6}He$
Summer 2026 OMEGA-60/OMEGA EP TNSA test of SLICS with $^{6}Li(t,p)^{8}Li$ (need enriched target)
Summer 2027 OMEGA-60 ^{6}Li doped high-yield tritium filled target $^{6}Li(t,p)^{8}Li$

VII. Talks and poster presentations since summer 2022

Mark Yuly, "**An Experiment Simulating the Production, Capture, and Detection of Nuclear Reaction Products from ICF**," Laboratory for Laser Energetics Experimental Physics Meeting, University of Rochester, Feb. 3, 2023.

Chunsun Lei, Andrew Hotchkiss, Andrew Martin, Adam Brown, Mark Yuly, James G. Mclean, Stephen J. Padalino, Chad J. Forrest, Thomas C. Sangster, Sean P. Regan, **"Depositing Lithium Films to Simulate ICF Reaction Products,"** OMEGA Laser User's Group Meeting, Laboratory for Laser Energetics, Rochester, NY, April 26, 2023;

XLI Annual Rochester Symposium for Physics Students, University of Rochester, April 15, 2023; 64th Annual Meeting of the APS Division of Plasma Physics, Spokane, WA, October 17-21, 2022.

Adam E. Brown, Andrew L. Martin, Mark Yuly, James G. McLean, Stephen J. Padalino, Chad J. Forrest, Thomas C. Sangster, Sean P. Regan, **"An Experiment Simulating the Production, Capture, and Detection of ^{8}Li from an ICF Implosion,"** OMEGA Laser User's Group Meeting, Laboratory for Laser Energetics, Rochester, NY, April 26, 2023; XLI Annual Rochester Symposium for Physics Students, University of Rochester, April 15, 2023; 64th Annual Meeting of the APS Division of Plasma Physics, Spokane, WA, October 17-21, 2022.

This material is based upon work supported by the Department of Energy [National Nuclear Security Administration] University of Rochester "National Inertial Confinement Program" under Award Number(s) DE-NA0004144.

This report was prepared as an account of work sponsored by an agency of the United States Government. Neither the United States Government nor any agency thereof, nor any of their employees, makes any warranty, express or implied, or assumes any legal liability or responsibility for the accuracy, completeness, or usefulness of any information, apparatus, product, or process disclosed, or represents that its use would not infringe privately owned rights. Reference herein to any specific commercial product, process, or service by trade name, trademark, manufacturer, or otherwise does not necessarily constitute or imply its endorsement, recommendation, or favoring by the United States Government or any agency thereof. The views and opinions of authors expressed herein do not necessarily state or reflect those of the United States Government or any agency thereof.

---

[1] Mark Yuly, Stephen Padalino, Micah Coates and Katelyn Cook, "A possible measurement of the 3H(t,γ)6He cross section at low energy," in Nuclear and Plasma Diagnostics for the EP-OMEGA and MTW Laser Systems, LLE Proposal for Subaward 416231-G, 2016 (unpublished).
[2] Mark Yuly, Stephen Padalino, Micah Coates and Katelyn Cook, "A Phoswich Detector System to Measure the 3H(t,□)6He Cross Section using ICF" in Nuclear and Plasma Diagnostics for the EP-OMEGA and MTW Laser Systems, LLE Proposal for Subaward 416231-G, 2017 (unpublished).
[3] Mark Yuly, Stephen Padalino, Emma Bruce, Katelyn Cook, and Sarah Hull, "Measuring Low Energy Nuclear Cross Sections using ICF," in Nuclear and Plasma Diagnostics for the EP-OMEGA and MTW Laser Systems, LLE Proposal for Subaward 416231-G, 2018 (unpublished).
[4] Mark Yuly, Stephen Padalino, Tyler Kowalewski, Salvatore Ferri and Steven Raymond, "Inertial Confinement Fusion as a Tool to Study Fundamental Nuclear Science," in Nuclear and Plasma Diagnostics for the EP-OMEGA and MTW Laser Systems, LLE Proposal for Subaward 416231-G, 2019 (unpublished).
[5] Mark Yuly, Stephen Padalino, Micah Christensen, Joshua Bowman, "Progress toward using ICF to measure light-ion nuclear cross sections" in Nuclear and Plasma Diagnostics for the EP-OMEGA and MTW Laser Systems, LLE Proposal for Subaward 416231-G, 2020 (unpublished).
[6] Mark Yuly, Stephen Padalino, Adam Brown, Micah Christensen, Micah Condie, "Trapping and detecting trace radioactive isotopes produced in ICF implosions," in Nuclear and Plasma Diagnostics for the EP-OMEGA and MTW Laser Systems, LLE Proposal for Subaward 416231-G, 2021 (unpublished).
[7] Mark Yuly, Stephen Padalino, Adam Brown, Andrew Hotchkiss, Chunsun Lei, Andrew Martin. "Trapping and detecting trace radioactive isotopes produced in ICF implosions," in Nuclear and Plasma Diagnostics for the EP-OMEGA and MTW Laser Systems, LLE Proposal for Subaward 416231-G, 2022 (unpublished).
[8] M. Roth and M. Schollmeier, in Proceedings of the CAS-CERN Accelerator School: Plasma Wake Acceleration, Geneva, Switzerland, 23–29 November 2014, edited by B. Holzer, CERN-2016-001 (CERN, Geneva, 2016).
[9] A.K. Schwemmlein, C. Stoeckl, C.J. Forrest, W.T. Shmayda, S.P. Regan, and W. U. Schröder, NIM B **522**, 27-31 (2022).
[10] L. Weissman, C. Broude, G. Goldring, R. Hadar, M. Hass, F. Schwamm, M. Shaanan, Nuc. Phys. A **630**, 678-688 (1998).
[11] A. J. Elwyn, R. E. Holland, C. N. Davids, and W. Ray, Jr., Phys. Rev. **C** 25, 2168 (1982).
[12] B. W. Filippone, A. J. Elwyn, W. Ray, Jr., and D. D. Koetke, Phys. Rev. C **25**, 2174 (1982).
[13] A.E. Schilling, N.F. Mangelson, K.K. Nielson, D.R. Dixon, M.W. Hill, G.L. Jensen, and V.C. Rogers, Nuc. Phys. A **263**, 389-396 (1976).
[14] Charles R. McClenahan and and Ralph E. Segel, Phys. Rev. C **11**, 370 (1975).
[15] Ralph W. Kavanagh, Nuc. Phys. **15**, 411-420 (1960).

[16] L. M. Baggett and S. J. Bame, Jr., Phys. Rev. **85,** 434 (1952).
[17] J.B. Woods and D.H. Wilkinson, Nuc. Phys. 61, 661-674 (1965).
[18] Stanley Bashkin, Phys. Rev. **95**, 1012 (1954).
[19] N. Otuka, et al., Nuclear Data Sheets 120, 272-276 (2014).
[20] Vedder, James F., High-Energy Beta Decay of Light Elements. Lawrence Berkeley National Laboratory Report UCRL8324 (1958).
[21] T. Sumikama, et. al., Phys. Rev. C **83**, 065501 (2011).
[22] J. Allison et al., Nucl. Instrum. Meth. A **835,** 186-225 (2016); J. Allison et al., IEEE Trans. Nucl. Sci. **53,** 270-278 (2006); S. Agostinelli et al., Nucl. Instrum. Meth. A **506,** 250-303 (2003).
[23] A.K. Schwemmlein, Ph.D. thesis (University of Rochester, 2021).
[24] A.K. Schwemmlein, W.T. Shmayda, C. Stoeckl , W.U. Schröder, and C. Mileham, NIM B **535**, 227-233 (2023).
[25] Abner Brenner, "Magnetic Method for Measuring the Thickness of Nonmagnetic Coatings on Iron and Steel," Journal of Research of the National Bureau of Standards, 20, 357 (1938). (National Bureau of Standards Research Paper RP1081)